THE JOURNAL OF PHYSICAL CHEMISTRY B

Article

pubs.acs.org/JPCB

Dynamical Correlation Effects on Photoisomerization: Ab Initio Multiple Spawning Dynamics with MS-CASPT2 for a Model *trans*-Protonated Schiff Base

Lihong Liu,[†,‡,§] Jian Liu,[‡,§,∥] and Todd J. Martinez*[,‡,§]

[†]Key Laboratory of Theoretical and Computational Photochemistry, Ministry of Education, College of Chemistry, Beijing Normal University, Beijing 100875, China

[‡]Department of Chemistry and PULSE Institute, Stanford University, Stanford, California 94305, United States

[§]SLAC National Accelerator Laboratory, Menlo Park, California 94309, United States

[∥]Beijing National Laboratory for Molecular Sciences, Institute of Theoretical and Computational Chemistry, College of Chemistry and Molecular Engineering, Peking University, Beijing 100871, China

Supporting Information

ABSTRACT: We investigate the photoisomerization of a model retinal protonated Schiff base (*trans*-PSB3) using *ab initio* multiple spawning (AIMS) based on multistate second order perturbation theory (MSPT2). Discrepancies between the photodynamical mechanism computed with three-root state-averaged complete active space self-consistent field (SA-3-CASSCF, which does not include dynamic electron correlation effects) and MSPT2 show that dynamic correlation is critical in this photoisomerization reaction. Furthermore, we show that the photodynamics of *trans*-PSB3 is not well-described by predictions based on minimum energy conical intersections (MECIs) or minimum energy conical intersection (CI) seam paths. Instead, most of the CIs involved in the photoisomerization are far from MECIs and minimum energy CI seam paths. Thus, both dynamical nuclear effects and dynamic electron correlation are critical to understanding the photochemical mechanism.

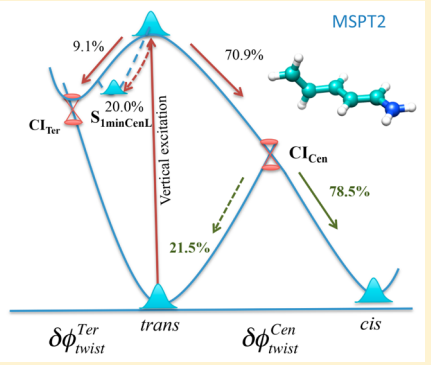

1. INTRODUCTION

Photoactive proteins in the rhodopsin family are driven by *cis*–*trans* photoisomerization of a retinal protonated Schiff base (RPSB) chromophore, achieving a variety of functions including photoreception and ion pumping. For example, bacteriorhodopsin acts as a photon-driven proton pump converting light energy into an electrochemical proton gradient through all-*trans* to 13-*cis* photoisomerization of RPSB.[1−7] The key role of RPSB photoisomerization in triggering the function of rhodopsins has spurred many experimental[7,8] and theoretical[8−22] investigations of the photodynamics in the CH_2-$(CH_2)_{n+1}NH_2^+$ (PSBn) model protonated Schiff bases. The *trans*-penta-2,4-dieniminium cation ($C_5H_8N^+$, *trans*-PSB3), which has only three conjugated double bonds, has attracted considerable theoretical interest as the simplest model for the photoisomerization mechanism in these systems.[9,14,16,17]

It has been shown that dynamic electronic correlation can have a significant effect on the geometric structures and energetics of minimal energy conical intersections (MECIs) in PSB3.[14,23,24] Since it has been well-established that conical intersections play a critical role in promoting nonadiabatic transitions and electronic quenching in photoisomerization,[25−28] this implies that accurate modeling of the photochemical mechanism and dynamics may need to go beyond simple multireference methods such as complete active space self-consistent field (CASSCF), which describe primarily static electron correlation. Unfortunately, this has been difficult because of computational expense, leading to the necessity of approximate treatments such as scaling of the CASSCF potential energy surface.[22]

In this paper, we report on nonadiabatic dynamics calculations of the excited state of PSB3 using multistate second order perturbation corrected CAS (MSPT2) to describe the underlying potential energy surfaces.[29] Energy gradients and nonadiabatic coupling vectors for MSPT2 are calculated analytically, as described previously.[30−32] Importantly, the MSPT2 method includes dynamic electron correlation and also allows the interaction of the correlated states that is necessary to describe the region near conical intersections correctly.

As has been discussed several times previously,[33−35] it is not at all straightforward to correctly describe the topography of potential energy surfaces around conical intersections. In general, single reference methods such as time-dependent density functional theory (TDDFT) and single excitation

Special Issue: Bruce C. Garrett Festschrift

Received: October 8, 2015
Revised: December 16, 2015
Published: December 17, 2015

DOI: 10.1021/acs.jpcb.5b09838
J. Phys. Chem. B 2016, 120, 1940−1949

configuration interaction (CIS) lead to severe difficulties because they cannot model a degenerate ground state. Although multireference methods can in principle describe such degeneracy, special care is needed when implementing perturbative corrections. Specifically, one must end with diagonalization of an effective Hamiltonian matrix in order that the "conical" topography can be maintained (as is done in MSPT2). The "conical" topography implies that there are exactly two molecular displacements which remove the degeneracy in first order (for a two-state intersection). When an intersection does not exhibit this conical topography, one often finds multiple closely spaced crossings, and this can lead to artificial population "sloshing" between the states. For example, instead of simple population transfer from the upper state to the lower state around the intersection, population transfer from the upper state to the lower state and shortly thereafter from the lower state back to the upper state has been observed.[36] Such complicated population dynamics could arise when the intersection topography was treated correctly, and thus, it is difficult to predict when this is an artifact of nonconical topography. This makes the description of nonadiabatic dynamics highly questionable when the underlying surfaces have incorrect intersection topography, as in the commonly used single state CASPT2 method (also often referred to as SS-CASPT2 or just CASPT2).[37]

The paper is organized as follows: Section 2 first summarizes the theoretical methods and presents computational details. Section 3 first describes the results of conventional time-independent quantum chemistry analysis of the potential energy surfaces, including local minima of PSB3 and minimum energy CI seam paths connecting different MECIs. We then present the results of *ab initio* nonadiabatic dynamics simulations using both CASSCF and MSPT2 to describe the potential energy surfaces and their couplings. Finally, concluding remarks are given in section 4.

2. THEORETICAL METHODS AND SIMULATION DETAILS

Electronic Structure and Stationary Point Characterization. Local minimum and MECI geometries have been optimized with both CASSCF and MSPT2 using a version of Molpro2006[38] which was locally modified to calculate analytic MSPT2 nonadiabatic couplings.[30,31] The active space contains six electrons in six orbitals, which includes all the π electrons and orbitals. The three lowest singlet electronic states are equally weighted in a state-averaged CASSCF procedure,[39,40] and the 6-31G basis set was used;[41,42] i.e., we use SA-3-CAS(6,6)/6-31G and SA-3-MS-CASPT2(6,6)/6-31G electronic wave functions. Basis set effects were assessed by optimizing stationary point and MECI geometries using the larger 6-31G* basis set. A level shift of 0.2 hartree was used in the MSPT2 method, and the 1s core orbitals of heavy atoms (C and N) are not correlated. The twist angle of PSB3, ϕ_{twist}, is defined by using angle trisectors.[43] The values that we report here are the changes in the twist angle, i.e., $\Delta\phi_{\text{twist}}$, compared to the equilibrium geometry of *trans*-PSB3 on the ground state (where $\phi_{\text{twist}} = 180°$ for all three double bonds). It is important to point out that CASSCF can be sensitive to both the number of electrons/orbitals in the active space and also to the number of states included in the average.[23,44] Although we average over three states for a consistent comparison of CASSCF and MSPT2, it is possible that the CASSCF results would be somewhat different if only two states were included in the averaging. Because it includes dynamic electron correlation, the MSPT2 method is usually not particularly sensitive to the number of states included in the averaging.

It is well-known that MECIs are not necessarily the most important points promoting nonadiabatic transitions along the intersection seam. Thus, it can be important to further characterize the intersection seam. We do this here with the seam space nudged elastic band (SS-NEB) method,[45] that finds minimal energy paths connecting two MECIs while maintaining the electronic state degeneracy. We characterize the seam paths connecting MECIs using both CASSCF and MSPT2. Seam path calculations at the MSPT2 level are performed with 14 uncorrelated orbitals (compared with only six uncorrelated orbitals corresponding to the 1s electrons of heavy atoms in other MSPT2 calculations used in this work). As shown in Supporting Information (Table S23), this has little effect on the relative energies of the MECIs, and thus is not expected to have a large effect on the seam paths.

It has been suggested that the topography around conical intersections might be an important indicator of their efficiency in promoting nonadiabatic transitions. For example, a "peaked" intersection could act as an efficient funnel, while a "sloped" intersection might be less effective.[46−50] We investigate this here, necessitating the introduction of parameters that can succinctly characterize the topography around an intersection. We use the framework introduced by Yarkony[48] for this purpose. Any conical intersection involving two degenerate electronic states can be characterized by the two molecular displacements that lift the degeneracy in first order, i.e., the branching plane vectors:

$$\mathbf{g}_{IJ} = \frac{1}{2}\left(\frac{\partial E_I}{\partial \mathbf{R}} - \frac{\partial E_J}{\partial \mathbf{R}}\right) \tag{1}$$

$$\mathbf{h}_{IJ} = \left\langle \phi_I \left| \frac{\partial H}{\partial \mathbf{R}} \right| \phi_J \right\rangle \tag{2}$$

The mixing of the two electronic wave functions ϕ_I and ϕ_J, which is arbitrary at a conical intersection where the two states are degenerate, is chosen to ensure the orthogonality of the branching plane vectors.[26] The branching plane can then be further characterized by the parameters d_{gh} and Δ_{gh}:

$$d_{gh} = \sqrt{(g^2 + h^2)} \tag{3}$$

$$\Delta_{gh} = \frac{g^2 - h^2}{d_{gh}^2} \tag{4}$$

Here g and h are the lengths of the orthogonal branching plane vectors. Finally, the topography of the conical intersection can be related to the "seam coordinate":

$$\mathbf{s}_{IJ} = \frac{\partial}{\partial \mathbf{R}}\left(\frac{E_I + E_J}{2}\right) \tag{5}$$

Yarkony then defined tilt parameters s_x and s_y as

$$s_x = \frac{\mathbf{s}_{IJ}\cdot\mathbf{g}_{IJ}}{g} \tag{6}$$

$$s_y = \frac{\mathbf{s}_{IJ}\cdot\mathbf{h}_{IJ}}{h} \tag{7}$$

DOI: 10.1021/acs.jpcb.5b09838
J. Phys. Chem. B 2016, 120, 1940−1949

which provide information about the degree of sloped/peaked character along each of the two branching plane directions. In order to make quantitative comparisons between different conical intersections, Yarkony introduced a length scaling to obtain

$$s^x = \frac{s_x}{g} = \frac{\mathbf{s}_{IJ}\cdot\mathbf{g}_{IJ}}{g^2} \tag{8}$$

$$s^y = \frac{s_y}{h} = \frac{\mathbf{s}_{IJ}\cdot\mathbf{h}_{IJ}}{h^2} \tag{9}$$

The four parameters d_{gh}, Δ_{gh}, s^x, and s^y suffice to specify the topography around a particular conical intersection.[48] The parameters d_{gh} and Δ_{gh} describe the sharpness and asymmetry of the intersection (the degree to which the conical intersection is ellipsoidal), respectively. The parameters s^x and s^y vanish for perfectly peaked (hourglass shaped) intersections, and larger values imply that the intersection is strongly sloped along the corresponding branching plane direction(s).

Nonadiabatic Dynamics. Since the full multiple spawning (FMS) method for nonadiabatic dynamics has been described in detail,[19,31,51−54] we limit ourselves to a brief summary here. The total electronic and nuclear wave function of a molecule in FMS is given as

$$\psi(\mathbf{r}, \mathbf{R}, t) = \sum_I \chi_I(\mathbf{R}, t)\phi_I(\mathbf{r}; \mathbf{R}) \tag{10}$$

where $\mathbf{R}/\mathbf{r}$ indicate nuclear/electronic coordinates, I is the electronic state index, and $\chi_I(\mathbf{R},t)/\phi_I(\mathbf{r};\mathbf{R})$ are nuclear/electronic wave functions, respectively. The nuclear wave functions for each electronic state are then expanded in a set of complex frozen Gaussian nuclear trajectory basis functions (TBFs)[55]

$$\chi_I(\mathbf{R}, t) = \sum_i c_I^i(t)\chi_I^i(\mathbf{R}; \bar{\mathbf{R}}_I^i(t), \bar{\mathbf{P}}_I^i(t), \gamma_I^i(t)) \tag{11}$$

each of which is characterized by a time-dependent mean position $\bar{\mathbf{R}}_I^i(t)$, mean momentum $\bar{\mathbf{P}}_I^i(t)$, and phase $\gamma_I^i(t)$. The complex coefficients $c_I^i(t)$ are determined by solving the fully coupled time-dependent Schrödinger equation in the basis set of TBFs. Each of the TBFs evolves on an adiabatic potential energy surface, following Hamilton's equations. The basis set is adaptively expanded during nonadiabatic transitions, through "spawning", in order to provide the needed TBFs evolving on a different electronic state. When FMS is implemented with "on the fly" solution of the electronic structure problem (energies, gradients, and nonadiabatic coupling vectors), it is typically referred to as *ab initio* multiple spawning (AIMS), which is the method used here.

We have carried out AIMS simulations of the dynamics of PSB3 after excitation to the lowest bright electronic state (S_1) using both MSPT2 and CASSCF in this work. The latter are provided for comparison, in order to assess the role of dynamic correlation effects in the nonadiabatic dynamics of PSB3. We find significant differences, as described below. Initial conditions are generated by randomly sampling from the Wigner distribution of the ground vibrational state in the harmonic approximation around the all-*trans* minimum on the ground electronic state (S_0). We use a time step of 20 atomic units (≈0.5 fs) to integrate the equations of motion for the TBFs and their complex coefficients. When the energy gap between two electronic states becomes small for any TBF, we switch to a smaller time step of 5 atomic units in order to ensure accurate integration of the quickly varying complex coefficients. The time step is adaptively adjusted to even smaller values if necessary, to ensure classical energy conservation for each TBF and norm conservation for the entire wave function during propagation. The dynamics is followed for 200 fs, which is sufficient for almost all of the population to reach the ground electronic state. We use 100 distinct initial conditions for the AIMS-SA3-CASSCF(6,6)/6-31G dynamics, leading to 651 TBFs after spawning. For the AIMS-SA3-MSPT2(6,6)/6-31G dynamics, we use 46 initial conditions, leading to 159 TBFs after spawning. Details of the electronic structure treatment are as given above; i.e., a level shift of 0.2 atomic units is used for MSPT2, and the six 1s orbitals are uncorrelated. As we are primarily interested in the excited state dynamics of PSB3 here, TBFs which reach the ground state are decoupled from other TBFs once their nonadiabatic coupling with other TBFs becomes negligible. These TBFs are then propagated independently until the final photoproduct can be identified on the basis of the twist angles around the single and double C−C bonds. It should be noted that we do not allow population transfer to the S_2 state in the AIMS-SA3-CASSCF(6,6)/6-31G dynamics because the AIMS-SA3-MSPT2(6,6)/6-31G dynamics reveals that the S_2 state is not involved in the population transfer dynamics. Allowing this population transfer would make the AIMS-SA3-CASSCF(6,6)/6-31G dynamics even more dramatically different from the AIMS-SA3-MSPT2(6,6)/6-31G dynamics.

3. RESULTS AND DISCUSSION

Stationary Structures and Their Relative Energies. Equilibrium structures of *trans*-PSB3 in the ground (S_0) and first excited (S_1) singlet states were optimized using SA3-CASSCF(6,6)/6-31G, SA3-MS-CASPT2(6,6)/6-31G, and SA3-MS-CASPT2(6,6)/6-31G*. The optimized structures are depicted in Figure 1 along with key geometric parameters (Cartesian coordinates are available in Supporting Information), and the relative energies are depicted in Figure 2. Relative energies with respect to the Franck−Condon (FC) point are listed in Table 1. Comparison of the MSPT2 structures obtained using the 6-31G and 6-31G* basis sets shows only minor differences. Thus, we focus primarily on results obtained with the 6-31G basis set (which is used in the dynamical simulations discussed below). As can be seen in Table 1, the lowest singlet excited state is optically bright in both CASSCF and MSPT2 calculations. The S_1 state involves considerable charge transfer from the C═N group to the terminal C═C group (as shown in more detail in Figure S1), in accord with previous investigations.[9,11,14] The CASSCF method overestimates the vertical excitation energy of S_1 in *trans*-PSB3, by approximately 16.5 kcal/mol compared to MSPT2.

Although we find several minima on the S_1 excited state at the CASSCF level, we find only a single S_1 minimum using MSPT2. In particular, at the CASSCF level, there are distinct S_1 minima corresponding to twisting about the terminal (S_{1min_Ter}), central (S_{1min_Cen}), and CN (S_{1min_CN}) double bonds. Each of the S_{1min_Cen}, S_{1min_CN}, and S_{min_Ter} CASSCF S_1 minima exhibits the expected bond-length alternation, as shown in Figure 1. At the MSPT2 level, all of the CASSCF S_1 minima are no longer stationary points, and there is a single distinct S_1 minimum (S_{1min_CenL}) with a geometry intermediate between the CASSCF S_{1min_Ter} and S_{1min_CenL} minima. The MSPT2 S_{1min_CenL} minimum involves systematic bond elongation

DOI: 10.1021/acs.jpcb.5b09838
J. Phys. Chem. B 2016, 120, 1940−1949

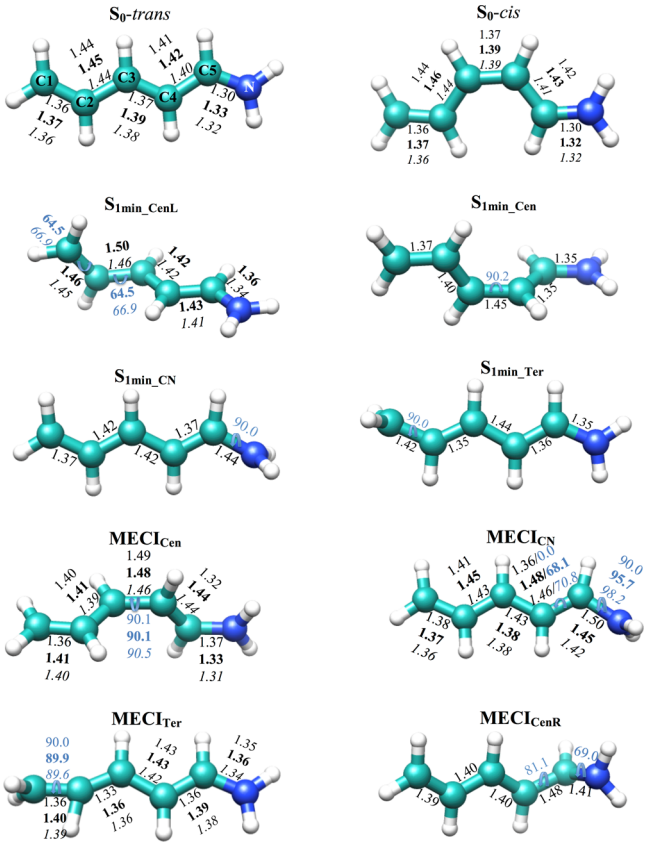

Figure 1. Stationary points of PSB3 located using SA3-CAS(6,6)/6-31G, MS-SA3-CASPT2(6,6)/6-31G (geometric parameters in bold), and MS-SA3-CASPT2(6,6)/6-31G* (geometric parameters in italic). Bond lengths are given in black text, and twist angles are given in blue text.

compared to that of the CASSCF minima (where typically only *the twisted bond* is significantly elongated). Thus, the S_1 potential energy surface is qualitatively changed by the inclusion of dynamic electronic correlation effects, in agreement with previous work.[23,24,35]

Both CASSCF and MSPT2 find three S_0/S_1 MECIs, labeled $MECI_{Cen}$, $MECI_{CN}$, and $MECI_{Ter}$. These correspond to structures that twist mainly around the central C═C bond, the C═N bond, and the terminal C═C bond, respectively. Additionally, CASSCF finds MECIs that are partially twisted about multiple bonds ($MECI_{CenR}$ and $MECI_{BP}$), corresponding to "hula-twist" or "bicycle-pedal" (Tables S22 and S15, respectively) type motion.[56−58] Both MSPT2 and CASSCF agree that the lowest energy of all these is the $MECI_{Cen}$ structure, twisted around the central C═C bond. At the MSPT2 level, its relative energy (compared to the S_0 Franck−Condon point) is 56.9/60.3 kcal/mol for the 6-31G/6-31G* basis sets, respectively. The twist angle around the central C═C bond is 90°, and the central C═C bond length is elongated to 1.48 Å.

However, there are significant differences between the MSPT2 and CASSCF results for the remaining MECIs. The MECI twisted about the C═N bond is the highest energy among all MECIs at the MSPT2 level. It leads to a highly twisted geometry, with 96° twisting around C═N and 68° twisting around the right C—C single bond. For comparison, at the CASSCF level, $MECI_{CN}$ has the second lowest energy among the MECIs, with 90° twisting around C═N. The $MECI_{Ter}$ structure given by MSPT2 is similar to that predicted by CASSCF, as shown in Figure 1. Both MSPT2 and CASSCF structures are twisted around the terminal C═C bond, with no twisting around other bonds. Table 1 and Figure 2 show that $MECI_{Ter}$ is the least energetically favorable among the MECIs at the CASSCF level while it has the second lowest energy at the MSPT2 level. As shown in Table 1 and Figure 2, the lowest energy MECIs at the CASSCF level are $MECI_{Cen}$ and $MECI_{CN}$, but at the MSPT2 level these are $MECI_{Cen}$ and $MECI_{Ter}$. The parameters characterizing the intersection topography for these dominant MECIs are given in Table 2. Although there is reasonable agreement on the topography around the $MECI_{Cen}$ S_0/S_1 intersection, MSPT2 predicts a more peaked topography compared to that of CASSCF (suggesting that nonadiabatic

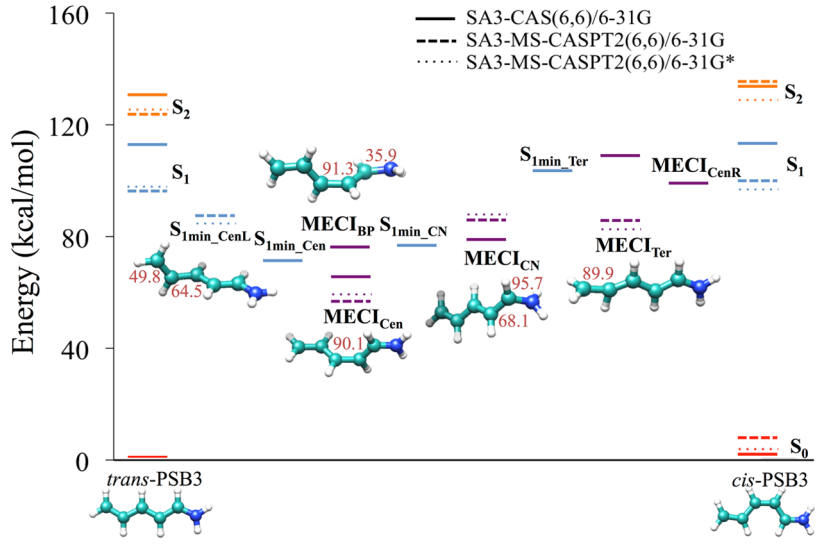

Figure 2. Energy-level diagram of minima and conical intersections of PSB3 at different potential energy surfaces with SA3-CAS(6,6)/6-31G, MS-SA3-CASPT2(6,6)/6-31G, and MS-SA3-CASPT2(6,6)/6-31G. Red/blue/orange colors denote the $S_0/S_1/S_2$ electronic state, respectively. Purple is used for geometries where S_0 and S_1 are degenerate.

DOI: 10.1021/acs.jpcb.5b09838
J. Phys. Chem. B 2016, 120, 1940−1949

Table 1. Relative Energies (in kcal/mol) of Stationary Point Geometries of PSB3 at the SA3-MS-CASPT2(6,6)/6-31G, SA3-MS-CASPT2(6,6)/6-31G*, and SA3-CASSCF(6,6)/6-31G levels

structure	SA3-CASSCF(6,6)/6-31G	SA3-MS-CASPT2(6,6)/6-31G	SA3-MS-CASPT2(6,6)/6-31G*
S_0-*trans*	0.0/113.2[a]/130.7[b]	0.0/96.7[a]/124.2[b]	0.0/98.3[a]/125.0[b]
osc str	−/1.10/0.09	−/1.25/0.02	−/1.24/0.01
S_0-*cis*	3.0/113.0[a]/133.9[b]	6.9/98.9[a]/134.8[b]	3.0/97.2[a]/128.5[b]
osc str	−/0.80/0.16	−/0.73/0.04	−/0.99/0.01
S_{1min_CenL}	95.2	87.5	85.1
S_{1min_Cen}	71.3		
S_{1min_CN}	77.7		
S_{1min_Ter}	104.0		
$MECI_{Cen}$	66.1	56.9	60.3
$MECI_{CN}$	79.1	86.3	87.8
$MECI_{Ter}$	108.9	85.4	82.7
$MECI_{CenR}$	99.4		

[a]Vertical excitation energy of 1st excited state relative to S_0-*trans*. [b]Vertical excitation energy of 2nd excited state relative to S_0-*trans*.

Table 2. Comparison of Intersection Topography for the Lowest-Lying S_0/S_1 MECIs of PSB3, with and without Dynamic Correlation

structure	s_x/g	s_y/h	Δ_{gh}	d_{gh}	s_x	s_y
$MECI_{Cen}$ (CAS)	−0.16	1.63	0.29	0.13	−0.02	0.12
$MECI_{CN}$ (CAS)	0.86	0.44	0.69	0.12	0.09	0.02
$MECI_{Cen}$ (MSPT2)	−0.24	1.15	0.70	0.16	−0.04	0.07
$MECI_{Ter}$ (MSPT2)	0.06	1.05	0.65	0.22	0.01	0.10

transitions might be expected to be more efficient when dynamic electron correlation is included).

Figure 3 shows the minimum energy CI seam path connecting the two lowest S_1/S_0 MECIs ($MECI_{Cen}$ and $MECI_{CN}$) at the SA3-CASSCF(6,6)/6-31G level. As will be shown below (and as expected from the energetics shown in Figure 2), these are the two MECIs which are most involved in the CASSCF nonadiabatic dynamics. Two regions of the MECI seam are energetically accessible after vertical Franck−Condon excitation. One of these regions exhibits ∼90° twisting around the central C═C bond with 0−70° twisting around the C═N bond. The other region exhibits ∼90° twisting around the C═N bond with 0−40° twisting around the central C═C bond. The intersections along the MECI seam in these energetically allowed regions are quite peaked, while the intersections along the MECI seam in energetically forbidden regions are quite sloped (further details in Table S24).

Figure 4 shows the minimum energy CI seam path connecting the two lowest S_1/S_0 MECIs ($MECI_{Ter}$ and $MECI_{Cen}$) at the MS-SA3-CASPT2(6,6)/6-31 level (using 14 core orbitals). Again, there are two energetically allowed regions along the MECI seam and the two MECIs which are most important in the MSPT2 dynamics to be discussed below. The first of these exhibits ∼90° twisting around the central C═C bond with 0−50° twisting around the terminal C═C bond. The second region exhibits ∼90° twisting around the terminal C═C bond with 0−30° twisting around the central C═C bond. Similar to the situation in Figure 3 (further details are available in Table S25), the intersections along the MECI seam in the energetically allowed region are quite peaked, while the intersections along the MECI seam in the energetically forbidden region are strongly sloped.

The structural data presented here reveal both similarities and significant differences in the potential energy surfaces predicted by CASSCF and MSPT2. This opens the question as

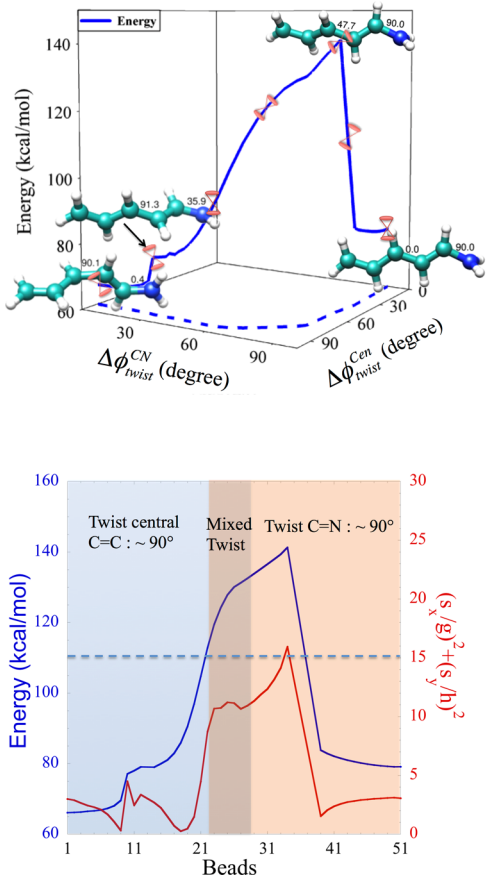

Figure 3. Minimum energy CI seam path connecting $MECI_{Cen}$ and $MECI_{CN}$ at the SA3-CAS(6,6)/6-31G level. All energies are relative to the S_0 energy at the Franck−Condon point. Upper panel: Projection of the MECI seam path along the two dominant twisting angles. Lower panel: Energy (blue) and slope parameter (red) profiles along the MECI seam path for each of the beads in the seam space nudged elastic band. The S_1 energy at the Franck−Condon point is indicated by the blue dashed line in the lower panel (only intersections lying below this dashed line are energetically accessible after vertical excitation).

to how different the dynamics predicted by these methods would be. This is especially important given that CASSCF studies of PSB3 (both static and dynamic) have formed the

DOI: 10.1021/acs.jpcb.5b09838
J. Phys. Chem. B 2016, 120, 1940−1949

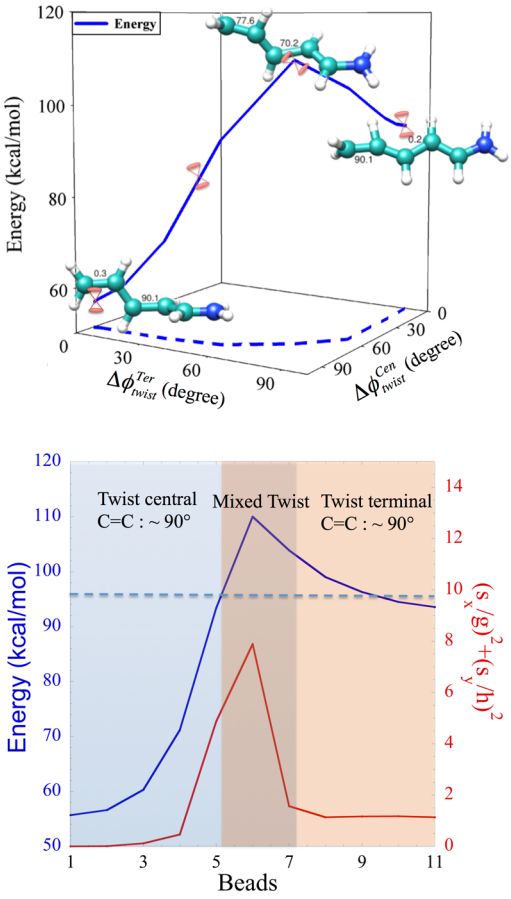

Figure 4. As in Figure 3, but for the minimum energy CI seam path connecting $MECI_{Ter}$ and $MECI_{Cen}$ at the MS-SA3-CASPT2(6,6)/6-31 level (using 14 core orbitals).

basis of much of the current understanding of photoisomerization in RPSB.[9,59]

AIMS Dynamics of PSB3. After photoexcitation, the initial relaxation motion of *trans*-PSB3 is dominated by stretching modes resulting in an elongation of the double bonds and contraction of the single bonds, i.e., bond-length alternation (BLA). As shown in Figure 5 (and further documented in Figure S2), this picture holds for both CASSCF and MSPT2 dynamics (although the amplitude of BLA motion is larger in CASSCF and the damping of this motion is stronger in MSPT2). Torsional motions begin to occur immediately after the initial BLA. This is in accord with the well-established two-mode relaxation model for the excited states of C=C double bonds.[59] In both CASSCF and MSPT2, the dominant outcome is torsion about the central C=C bond, and this leads to nonadiabatic transitions to the ground electronic state (*vide infra*). However, this is not the only observed pathway in either CASSCF or MSPT2. As shown in Table 3, CASSCF dynamics predicts that a significant fraction of the population decays by twisting about the C—N bond, in addition to small amounts that decay to S_0 through torsion about other single and double bonds. At the CASSCF level, the only bond which is not observed to twist significantly after photoexcitation is the terminal C=C bond. In contrast, the MSPT2 dynamics predicts that the only minor channel is torsion about the terminal C=C bond.

The excited state lifetime of PSB3 is similar at the MSPT2 and CASSCF levels, as shown in Figure 6a, with a time constant

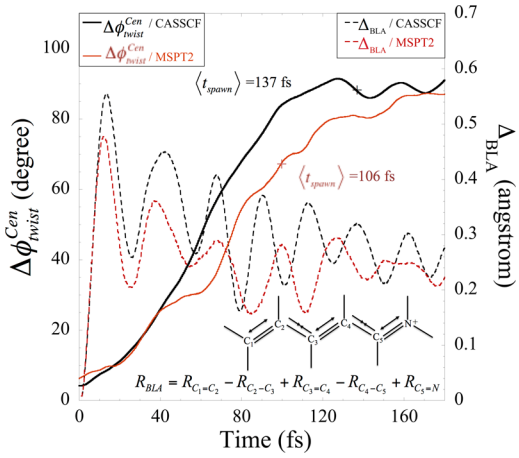

Figure 5. Time evolution after photoexcitation to S_1 for the twist angle around the central C=C bond (solid lines) and the bond-length alternation (BLA, dashed lines) at the SA3-CAS(6,6)/6-31G (black) and MS-SA3-CASPT2(6,6)/6-31G (red) levels. Results are averaged over TBFs which twist about the central C=C bond (see Figure S2 for details about other twist angles).

of ≈150 fs. Population transfer does not begin immediately, but instead there is a latency time corresponding to the time it takes to begin torsion about one of the bonds and thus to approach the CI seam. This latency time is shorter in CASSCF (≈20 fs) compared to MSPT2 (≈50 fs). The origin of this difference is the propensity for twisting about the C=N bond in CASSCF, which occurs more quickly than isomerization about other bonds (compare Figure S2 with Figure 5). This is also evident in Figure 6b; we show the excited state population as a function of time for the subset of TBFs which isomerize about the central C=C bond (which is the major channel in both CASSCF and MSPT2). For CASSCF, comparison with Figure 6a shows that the quenching latency for this subset is substantially longer than that for the total population trace. This indicates that it is torsion about the C=N bond which leads to a shorter quenching latency in CASSCF compared to that of MSPT2. We also note that for this majority decay channel (isomerization about the central C=C bond), the excited state quenching is faster in MSPT2. This is consistent with the more peaked character of the relevant $MECI_{Cen}$ in MSPT2 as discussed above.

Using both CASSCF and MSPT2, the AIMS simulations predict that the dominant quenching mechanism in *trans*-PSB3 is due to torsion about the C=C bond. This major channel is more dominant (89% of the time) in MSPT2 compared to CASSCF (76% of the time). We now turn to a more detailed analysis of the nonadiabatic process. In Figure 7, we show the propensity for and efficiency of nonadiabatic transitions as a function of the two most important torsional coordinates, the central C=C bond and the $C{=}N/C{=}C_{terminal}$ bond for CASSCF/MSPT2, respectively. Note that we choose a different second torsion angle in CASSCF and MSPT2 because the minor channel is different for these two cases, as discussed above. The upper panel of Figure 7 shows the distribution on S_1 that spawns to S_0. For each initial condition, this distribution consists of a population-weighted sum of the density for S_1 TBFs (often referred to as the "parent TBFs") at the "spawning time", when the nonadiabatic coupling is maximal. These distributions are then averaged over all initial conditions. The relevant MECIs (and the CI seam) are marked on the figure,

DOI: 10.1021/acs.jpcb.5b09838
J. Phys. Chem. B 2016, 120, 1940−1949

Table 3. Fraction of S_0 Population That Underwent Nonadiabatic Transitions from S_1 through Torsion about Different Bonds

twisting bonds	SA3-CASSCF(6,6)/6-31G	SA3-MS-CASPT2(6,6)/6-31G
terminal C═C		11 ± 9%
central C═C	76 ± 3%	89 ± 1%
C═N	23 ± 4%	
right C—C	0.5%[a]	
central C═C and C═N	0.2 ± 2%	
right C—C and C═N	0.5 ± 8%	

[a]Only one trajectory, no error bar has been calculated.

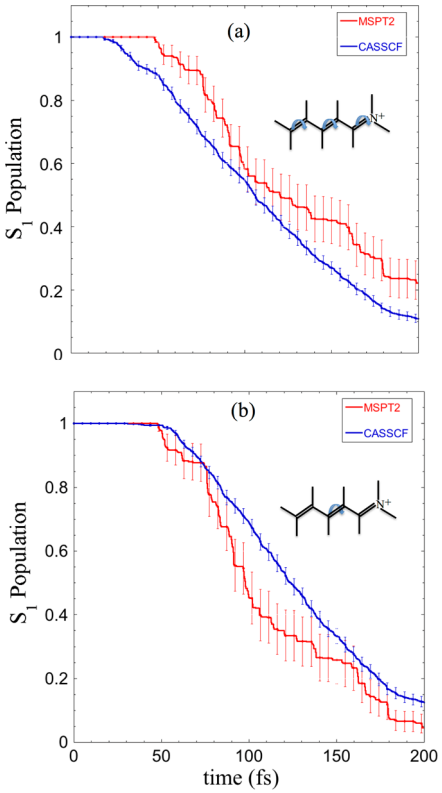

Figure 6. (a) Population dynamics of isolated *trans*-PSB3 after photoexcitation using SA3-CAS(6,6)/6-31G (blue) and MS-SA3-CASPT2(6,6)/6-31G (red). (b) Population dynamics for the subset of TBFs which twist about the central C═C bond after photoexcitation.

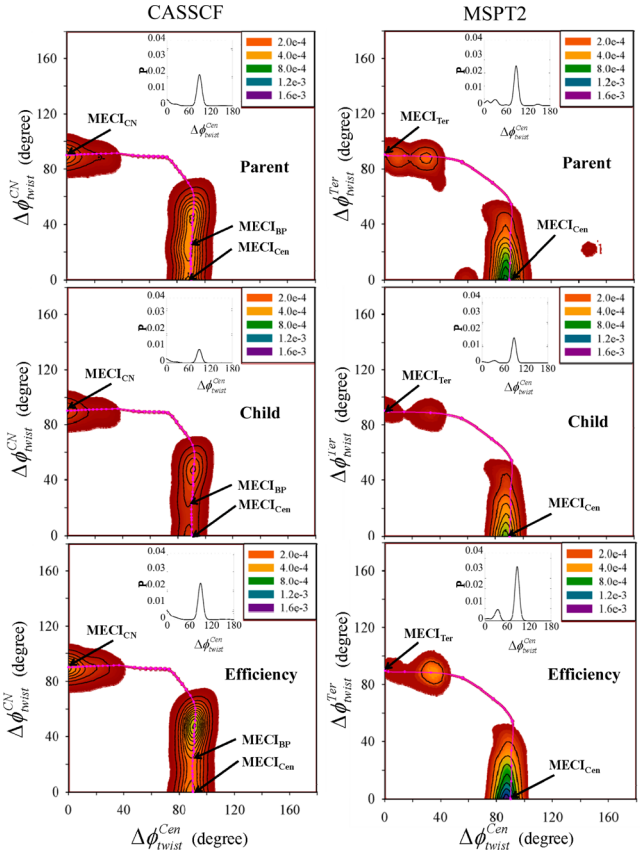

Figure 7. Distribution of spawning geometries projected on twisting around the central C═C and C═N bonds at the SA3-CAS(6,6)/6-31G level (left panels), and projected on twisting around the central and terminal C═C bonds at the MS-SA3-CASPT2(6,6)/6-31G level (right panels). Insets show the distributions projected on the central C═C bond twisting coordinate. Upper panels correspond to the distribution of the S_1 TBFs ("parent TBFs"). Middle panels correspond to the distribution of spawned TBFs on S_0 ("child TBFs"). Lower panels correspond to the transition efficiency. Nonadiabatic transitions are more efficient in MSPT2 and also concentrated more strongly near the $MECI_{Cen}$ geometry.

and one can see that, in both the CASSCF and MSPT2 cases, the population that spawns to S_0 is broadly distributed along the seam. Thus, the minimal energy conical intersection is not a good descriptor of the location of nonadiabatic transitions. In the middle panel of Figure 7, we show the population that quenches to S_0 as a result of the spawning. For each initial condition, this distribution is constructed as the population-weighted sum of all the TBFs spawned to S_0 ("child TBFs"). The population that is assigned to each of these child TBFs corresponds to the population of the TBF at the end of the nonadiabatic event (when the TBF exits the spawning region, i.e., when the nonadiabatic coupling becomes insignificant). The presented distribution is averaged over all initial conditions. As can be seen from the middle panel, this "child distribution" is again broadly distributed along the CI seam, further buttressing the conclusion that nonadiabatic transitions often occur far from an MECI (but in this case generally close to the CI seam). Finally, it is interesting to ask about the relative efficiency of nonadiabatic transitions at different points along the seam. The lower panel of Figure 7 shows the distribution of transition efficiency, defined as the distribution of spawning TBFs weighted by the ratio of the child and parent populations (the former is evaluated at the end of the nonadiabatic event, and the latter is evaluated at the beginning of the nonadiabatic event). Transitions mediated by torsion about the central C═C bond are much more efficient in MSPT2 compared to CASSCF. This is consistent with the earlier observation (*vide supra*) that the $MECI_{Cen}$ topography is more peaked in MSPT2 compared to CASSCF.

Figure 8 presents a schematic summary of *trans*-PSB3 photodynamics in the first 200 fs as predicted by AIMS/

DOI: 10.1021/acs.jpcb.5b09838
J. Phys. Chem. B 2016, 120, 1940−1949

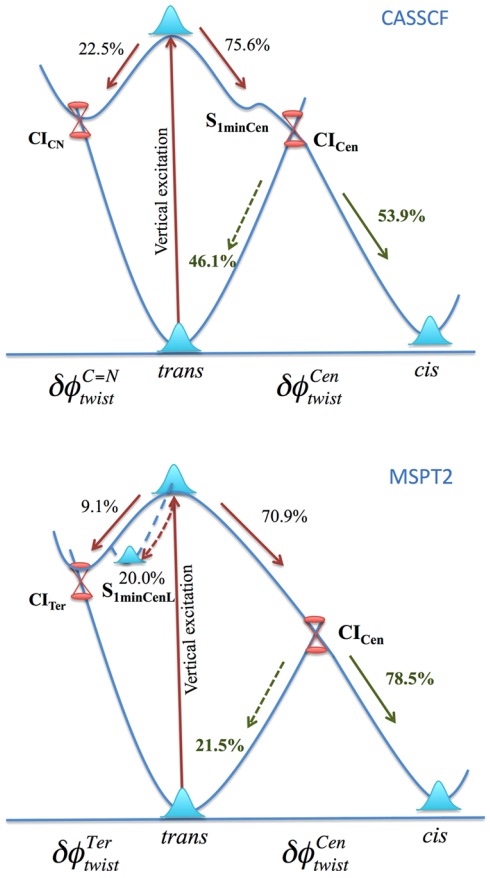

Figure 8. Scheme for the excited state reaction mechanism of PSB3 using SA3-CAS(6,6)/6-31G (upper panel) and MS-SA3-CASPT2-(6,6)/6-31G (lower panel). Note that the population which proceeds to $S_{1minCenL}$ in MSPT2 ultimately isomerizes about the terminal or central C═C bonds.

CASSCF (upper panel) and AIMS/MSPT2 (lower panel). Both CASSCF and MSPT2 predict that the dominant outcome is torsion about the central C═C bond. However, there are several differences that should be emphasized. First, the minor channels are completely different, with MSPT2 predicting torsion about the terminal C═C bond and CASSCF instead predicting torsion about the C═N bond. Second, there is an S_1 minimum in CASSCF along the way to $MECI_{Cen}$. This leads to a more sloped character of this MECI compared to MSPT2. Consequently, the population which decays to S_0 through torsion about the central C═C bond in CASSCF splits almost equally between *cis* and *trans* products. In contrast, there is no such minimum in MSPT2, and the result is a significant difference in the photoisomerization quantum yield for the population which isomerizes through torsion about the central C═C bond. Indeed, the combination of fast torsion, no intervening minimum, and a peaked intersection leads to 79% of the population forming the *cis* photoproduct.

4. CONCLUSIONS

In this paper we have compared the photodynamics of *trans*-PSB3 as predicted by SA-3-CASSCF and SA-3-MSPT2. Some aspects of the dynamics are quite similar, such as the dominant role of torsion about the central C═C bond in promoting electronic quenching. These aspects support the picture of RPSB photoisomerization that has been developed using this model system, including the two-state two-mode relaxation model.[59] However, there are also some important differences. Some of these could have been partially anticipated on the basis of minima and MECIs alone. For example, there are a number of distinct local minima on S_1 in CASSCF, but only a single S_1 local minimum in MSPT2. Furthermore, the energetics and topography of the MECIs are quite different in CASSCF and MSPT2. Carrying out the dynamical simulations shows the detailed impact of these differences. Many minor channels are observed in CASSCF, and the primary minor channel corresponds to torsion about the C═N bond. In MSPT2, there is a single minor channel, and it corresponds to torsion about the terminal C═C bond. Furthermore, the MECI corresponding to the dominant decay channel (isomerization about the central C═C bond) is more peaked in MSPT2 than in CASSCF. As a consequence, the nonadiabatic transitions are more efficient in MSPT2, and the *cis*:*trans* photoisomerization quantum yield deviates significantly from the 1:1 ratio predicted by CASSCF.

We also showed that, in both CASSCF and MSPT2, the nonadiabatic transitions often occur far from a MECI. Nevertheless, the MECI geometries are still useful, as they provide natural anchor points for seam paths (minimal energy paths in the intersection space) that can better describe the dynamics.

This work shows that dynamic electron correlation can be quite important in excited state dynamics and motivates further work to incorporate dynamic correlation routinely in photochemical studies. In the case of *trans*-PSB3, incorporating dynamic electron correlation into the photochemistry leads to significant changes in the predicted reaction pathways, the efficiency of population transfer, and the product quantum yield. Although we believe that the reported features of the AIMS-MSPT2 dynamics should be quite reliable, the benchmark status of PSB3 also makes it important to extend these results to more accurate electronic structure methods.[60,61] This remains for future work. We hope that this work will also motivate experiments on this model system for photoisomerization.

■ ASSOCIATED CONTENT

Supporting Information

The Supporting Information is available free of charge on the ACS Publications website at DOI: 10.1021/acs.jpcb.5b09838.

Detailed coordinates for molecular structures corresponding to optimized minima and MECIs, analysis of electronic wave functions at the Franck−Condon point, further details of relative energies of stationary points and MECIs, and further details of intersection topography along seam paths (PDF)

■ AUTHOR INFORMATION

Corresponding Author

*E-mail: Todd.Martinez@stanford.edu. Phone: 650-736-8860.

Notes

The authors declare no competing financial interest.

■ ACKNOWLEDGMENTS

This work was supported by the AMOS program within the Chemical Sciences, Geosciences and Biosciences Division of the Office of Basic Energy Sciences, Office of Science, US Department of Energy, and by a scholarship from the China Scholarship Council (CSC) under Grant CSC No.

DOI: 10.1021/acs.jpcb.5b09838
J. Phys. Chem. B 2016, 120, 1940−1949

20110604097. The authors thank T. Mori for helpful discussions.

REFERENCES

(1) Baudry, J.; Tajkhorshid, E.; Molnar, F.; Phillips, J.; Schulten, K. Molecular Dynamics Study of Bacteriorhodopsin and the Purple Membrane. *J. Phys. Chem. B* **2001**, *105*, 905−918.

(2) Edholm, O.; Berger, O.; Jahnig, F. Structure and Fluctuations of Bacteriorhodopsin in the Purple Membrane - a Molecular Dynamics Study. *J. Mol. Biol.* **1995**, *250*, 94−111.

(3) Lanyi, J. K. Bacteriorhodopsin. *Annu. Rev. Physiol.* **2004**, *66*, 665−688.

(4) Pebay-Peyroula, E.; Rummel, G.; Rosenbusch, J. P.; Landau, E. M. X-Ray Structure of Bacteriorhodopsin at 2.5 Angstroms from Microcrystals Grown in Lipidic Cubic Phases. *Science* **1997**, *277*, 1676−1681.

(5) Schulten, K.; Humphrey, W.; Logunov, I.; Sheves, M.; Xu, D. Molecular Dynamics Studies of Bacteriorhodopsin's Photocycles. *Isr. J. Chem.* **1995**, *35*, 447−464.

(6) Tajkhorshid, E.; Baudry, J.; Schulten, K.; Suhai, S. Molecular Dynamics Study of the Nature and Origin of Retinal's Twisted Structure in Bacteriorhodopsin. *Biophys. J.* **2000**, *78*, 683−693.

(7) Yen, C. W.; Hayden, S. C.; Dreaden, E. C.; Szymanski, P.; El-Sayed, M. A. Tailoring Plasmonic and Electrostatic Field Effects to Maximize Solar Energy Conversion by Bacteriorhodopsin, the Other Natural Photosynthetic System. *Nano Lett.* **2011**, *11*, 3821−3826.

(8) Sovdat, T.; Bassolino, G.; Liebel, M.; Schnedermann, C.; Fletcher, S. P.; Kukura, P. Backbone Modification of Retinal Induces Protein-Like Excited State Dynamics in Solution. *J. Am. Chem. Soc.* **2012**, *134*, 8318−8320.

(9) Garavelli, M.; Celani, P.; Bernardi, F.; Robb, M. A.; Olivucci, M. The $C_5H_6NH_2^+$ Protonated Shiff Base: An Ab Initio Minimal Model for Retinal Photoisomerization. *J. Am. Chem. Soc.* **1997**, *119*, 6891−6901.

(10) Aquino, A. J. A.; Barbatti, M.; Lischka, H. Excited-State Properties and Environmental Effects for Protonated Schiff Bases: A Theoretical Study. *ChemPhysChem* **2006**, *7*, 2089−2096.

(11) Cembran, A.; Bernardi, F.; Olivucci, M.; Garavelli, M. Counterion Controlled Photoisomerization of Retinal Chromophore Models: A Computational Investigation. *J. Am. Chem. Soc.* **2004**, *126*, 16018−16037.

(12) Li, X.; Chung, L. W.; Morokuma, K. Photodynamics of All-Trans Retinal Protonated Schiff Base in Bacteriorhodopsin and Methanol Solution. *J. Chem. Theory Comput.* **2011**, *7*, 2694−2698.

(13) Migani, A.; Sinicropi, A.; Ferre, N.; Cembran, A.; Garavelli, M.; Olivucci, M. Structure of the Intersection Space Associated with Z/E Photoisomerization of Retinal in Rhodopsin Proteins. *Faraday Discuss.* **2004**, *127*, 179−191.

(14) Mori, T.; Nakano, K.; Kato, S. Conical Intersections of Free Energy Surfaces in Solution: Effect of Electron Correlation on a Protonated Schiff Base in Methanol Solution. *J. Chem. Phys.* **2010**, *133*, 064107.

(15) Munoz-Losa, A.; Martin, M. E.; Galvan, I. F.; Sanchez, M. L.; Aguilar, M. A. Solvent Effects on the Radiative and Nonradiative Decay of a Model of the Rhodopsin Chromophore. *J. Chem. Theory Comput.* **2011**, *7*, 4050−4059.

(16) Ruckenbauer, M.; Barbatti, M.; Muller, T.; Lischka, H. Nonadiabatic Excited-State Dynamics with Hybrid Ab Initio Quantum-Mechanical/Molecular-Mechanical Methods: Solvation of the Pentadieniminium Cation in Apolar Media. *J. Phys. Chem. A* **2010**, *114*, 6757−6765.

(17) Szymczak, J. J.; Barbatti, M.; Lischka, H. Mechanism of Ultrafast Photodecay in Restricted Motions in Protonated Schiff Bases: The Pentadieniminium Cation. *J. Chem. Theory Comput.* **2008**, *4*, 1189−1199.

(18) Valsson, O.; Filippi, C. Photoisomerization of Model Retinal Chromophores: Insight from Quantum Monte Carlo and Multi-configurational Perturbation Theory. *J. Chem. Theory Comput.* **2010**, *6*, 1275−1292.

(19) Virshup, A. M.; Punwong, C.; Pogorelov, T. V.; Lindquist, B. A.; Ko, C.; Martinez, T. J. Photodynamics in Complex Environments: Ab Initio Multiple Spawning Quantum Mechanical/Molecular Mechanical Dynamics. *J. Phys. Chem. B* **2009**, *113*, 3280−3291.

(20) Barbatti, M.; Ruckenbauer, M.; Szymczak, J. J.; Aquino, A. J. A.; Lischka, H. Nonadiabatic Excited-State Dynamics of Polar Pi-Systems and Related Model Compounds of Biological Relevance. *Phys. Chem. Chem. Phys.* **2008**, *10*, 482−494.

(21) Warshel, A.; Chu, Z. T. Nature of the Surface Crossing Process in Bacteriorhodopsin: Computer Simulations of the Quantum Dynamics of the Primary Photochemical Event. *J. Phys. Chem. B* **2001**, *105*, 9857−9871.

(22) Frutos, L. M.; Andruniow, T.; Santoro, F.; Ferre, N.; Olivucci, M. Tracking the Excited-State Time Evolution of the Visual Pigment with Multiconfigurational Quantum Chemistry. *Proc. Natl. Acad. Sci. U. S. A.* **2007**, *104*, 7764−7769.

(23) Gozem, S.; Huntress, M.; Schapiro, I.; Lindh, R.; Granovsky, A. A.; Angeli, C.; Olivucci, M. Dynamic Electron Correlation Effects on the Ground State Potential Energy Surface of a Retinal Chromophore Model. *J. Chem. Theory Comput.* **2012**, *8*, 4069−4080.

(24) Gozem, S.; Melaccio, F.; Lindh, R.; Krylov, A. I.; Granovsky, A. A.; Angeli, C.; Olivucci, M. Mapping the Excited State Potential Energy Surface of a Retinal Chromophore Model with Multireference and Equation-of-Motion Coupled-Cluster Methods. *J. Chem. Theory Comput.* **2013**, *9*, 4495−4506.

(25) Levine, B. G.; Martinez, T. J. Isomerization through Conical Intersections. *Annu. Rev. Phys. Chem.* **2007**, *58*, 613−634.

(26) Yarkony, D. R. Conical Intersections: The New Conventional Wisdom. *J. Phys. Chem. A* **2001**, *105*, 6277−6293.

(27) Robb, M. A.; Bernardi, F.; Olivucci, M. Conical Intersections as a Mechanistic Feature of Organic Photochemistry. *Pure Appl. Chem.* **1995**, *67*, 783−789.

(28) Garavelli, M.; Bernardi, F.; Olivucci, M.; Vreven, T.; Klein, S.; Celani, P.; Robb, M. A. Potential-Energy Surfaces for Ultrafast Photochemistry. *Faraday Discuss.* **1998**, *110*, 51−70.

(29) Finley, J.; Malmqvist, P.-A.; Roos, B. O.; Serrano-Andres, L. The Multi-State CASPT2 Method. *Chem. Phys. Lett.* **1998**, *288*, 299−306.

(30) Mori, T.; Kato, S. Dynamic Electron Correlation Effect on Conical Intersections in Photochemical Ring-Opening Reaction of Cyclohexadiene: MS-CASPT2 Study. *Chem. Phys. Lett.* **2009**, *476*, 97−100.

(31) Mori, T.; Glover, W. J.; Schuurman, M. S.; Martinez, T. J. Role of Rydberg States in the Photochemical Dynamics of Ethylene. *J. Phys. Chem. A* **2012**, *116*, 2808−2818.

(32) Celani, P.; Werner, H.-J. Analytical Energy Gradients for Internally-Contracted Second-Order Multireference Perturbation Theory. *J. Chem. Phys.* **2003**, *119*, 5044−5057.

(33) Yang, S.; Martinez, T. J. Ab Initio Multiple Spawning: First Principles Dynamics around Conical Intersections. In *Conical Intersections: Theory, Computation and Experiment*; Domcke, W., Koppel, H., Eds.; World Scientific: Singapore, 2011.

(34) Levine, B. G.; Ko, C.; Quenneville, J.; Martinez, T. J. Conical Intersections and Double Excitations in Time-Dependent Density Functional Theory. *Mol. Phys.* **2006**, *104*, 1039−1051.

(35) Gozem, S.; Melaccio, F.; Valentini, A.; Filatov, M.; Huix-Rotllant, M.; Ferre, N.; Frutos, L. M.; Angeli, C.; Krylov, A. I.; Granovsky, A. A.; Lindh, R.; Olivucci, M. Shape of Multireference, Equation-of-Motion Coupled-Cluster, and Density Functional Theory Potential Energy Surfaces at a Conical Intersection. *J. Chem. Theory Comput.* **2014**, *10*, 3074−3084.

(36) Tapavicza, E.; Tavernelli, I.; Rothlisberger, U.; Filippi, C.; Casida, M. E. Mixed Time-Dependent Density-Functional Theory/Classical Trajectory Surface Hopping Study of Oxirane Photochemistry. *J. Chem. Phys.* **2008**, *129*, 124108.

(37) Roos, B. O. Theoretical Studies of Electronically Excited States of Molecular Systems Using Multiconfigurational Perturbation Theory. *Acc. Chem. Res.* **1999**, *32*, 137−144.

(38) Werner, H.-J.; Knowles, P. J.; Lindh, R.; Manby, F.; Schuetz, M. *Molpro, V2006.2*.

DOI: 10.1021/acs.jpcb.5b09838
J. Phys. Chem. B 2016, 120, 1940−1949

(39) Werner, H.-J.; Knowles, P. J. A Second-Order Multiconfiguration SCF Procedure with Optimum Convergence. *J. Chem. Phys.* **1985**, *82*, 5053−5063.
(40) Knowles, P. J.; Werner, H.-J. An Efficient Second-Order MCSCF Method for Long Configuration Expansions. *Chem. Phys. Lett.* **1985**, *115*, 259−267.
(41) Hehre, W. J.; Ditchfield, R.; Pople, J. A. Self-Consistent Molecular Orbital Methods. Xii. Further Extensions of Gaussian-Type Basis Sets for Use in Molecular Orbital Studies of Organic Molecules. *J. Chem. Phys.* **1972**, *56*, 2257−2261.
(42) Frisch, M. J.; Pople, J. A.; Binkley, J. S. Self-Consistent Molecular Orbital Methods. 25. Supplementary Functions for Gaussian Basis Sets. *J. Chem. Phys.* **1984**, *80*, 3265−3269.
(43) Evenhuis, C.; Martinez, T. J. A Scheme to Interpolate Potential Energy Surfaces and Derivative Coupling Vectors without Performing a Global Diabatization. *J. Chem. Phys.* **2011**, *135*, 224110.
(44) Levine, B. G.; Martinez, T. J. Ab Initio Multiple Spawning Dynamics of Excited Butadiene: Role of Charge Transfer. *J. Phys. Chem. A* **2009**, *113*, 12815−12824.
(45) Mori, T.; Martinez, T. J. Exploring the Conical Intersection Seam: The Seam Space Nudged Elastic Band Method. *J. Chem. Theory Comput.* **2013**, *9*, 1155−1163.
(46) Atchity, G. J.; Xantheas, S. S.; Ruedenberg, K. Potential Energy Surfaces near Intersections. *J. Chem. Phys.* **1991**, *95*, 1862−1876.
(47) Ben-Nun, M.; Molnar, F.; Schulten, K.; Martinez, T. J. The Role of Intersection Topography in Bond Selectivity of Cis-Trans Photoisomerization. *Proc. Natl. Acad. Sci. U. S. A.* **2002**, *99*, 1769−1773.
(48) Yarkony, D. R. Nuclear Dynamics near Conical Intersections in the Adiabatic Representation: I. The Effects of Local Topography on Interstate Transitions. *J. Chem. Phys.* **2001**, *114*, 2601−2613.
(49) Virshup, A. M.; Chen, J.; Martinez, T. J. Nonlinear Dimensionality Reduction for Nonadiabatic Dynamics: The Influence of Conical Intersection Topography on Population Transfer Rates. *J. Chem. Phys.* **2012**, *137*, 22A519.
(50) Malhado, J. P.; Hynes, J. T. Photoisomerization for a Model Protonated Schiff Base in Solution: Sloped/Peaked Conical Intersection Perspective. *J. Chem. Phys.* **2012**, *137*, 22A543.
(51) Ben-Nun, M.; Martinez, T. J. Nonadiabatic Molecular Dynamics: Validation of the Multiple Spawning Method for a Multidimensional Problem. *J. Chem. Phys.* **1998**, *108*, 7244−7257.
(52) Ben-Nun, M.; Quenneville, J.; Martinez, T. J. Ab Initio Multiple Spawning: Photochemistry from First Principles Quantum Molecular Dynamics. *J. Phys. Chem. A* **2000**, *104*, 5161−5175.
(53) Levine, B. G.; Coe, J. D.; Virshup, A. M.; Martinez, T. J. Implementation of Ab Initio Multiple Spawning in the Molpro Quantum Chemistry Package. *Chem. Phys.* **2008**, *347*, 3−16.
(54) Martinez, T. J.; Ben-Nun, M.; Ashkenazi, G. Classical/Quantal Method for Multi-State Dynamics: A Computational Study. *J. Chem. Phys.* **1996**, *104*, 2847−2856.
(55) Heller, E. J. Frozen Gaussians: A Very Simple Semiclassical Approximation. *J. Chem. Phys.* **1981**, *75*, 2923−2931.
(56) Warshel, A. Bicylce-Pedal Model for the First Step in the Vision Process. *Nature* **1976**, *260*, 679−683.
(57) Sumita, M.; Saito, K. Theoretical Study on Hula-Twist Motion of Penta-2,4-Dieniminium on the S_1 Surface under Isolated Condition by the Complete Active Space Self-Consistent Field Theory. *Chem. Phys. Lett.* **2006**, *424*, 374−378.
(58) Liu, R. S. H. Photoisomerization by Hula-Twist. Photoactive Biopigments. *Pure Appl. Chem.* **2002**, *74*, 1391−1396.
(59) Gonzalez-Luque, R.; Garavelli, M.; Bernardi, F.; Merchan, M.; Robb, M. A.; Olivucci, M. Computational Evidence in Favor of a Two-State, Two-Mode Model of the Retinal Chromophore Photisomerization. *Proc. Natl. Acad. Sci. U. S. A.* **2000**, *97*, 9379−9384.
(60) Shiozaki, T.; Gyorffy, W.; Celani, P.; Werner, H.-J. Extended Multi-State Complete Active Space Second-Order Perturbation Theory: Energy and Nuclear Gradients. *J. Chem. Phys.* **2011**, *135*, 081106.
(61) Granovsky, A. A. Extended Multi-Configuration Quasi-Degenerate Perturbation Theory: The New Approach to Multi-State Multi-Reference Perturbation Theory. *J. Chem. Phys.* **2011**, *134*, 214113.

DOI: 10.1021/acs.jpcb.5b09838
J. Phys. Chem. B 2016, 120, 1940−1949